Article

Photocatalytic Performance of SiO$_2$/CNOs/TiO$_2$ to Accelerate the Degradation of Rhodamine B under Visible Light

Weike Zhang [1,*,†], Yanrong Zhang [1,†], Kai Yang [2], Yanqing Yang [1,*], Jia Jia [1] and Lijun Guo [1]

[1] School of Environmental Science and Engineering, Taiyuan University of Technology, Taiyuan 030024, China; zhangyanrong0696@link.tyut.edu.cn (Y.Z.); jiajia6328@163.com (J.J.); 15234845580@163.com (L.G.)

[2] Laboratory for Earth Surface Processes, College of Urban and Environmental Sciences, Peking University, Beijing 100871, China; yangkai@pku.edu.cn

* Correspondence: zhangweike@tyut.edu.cn (W.Z.); yangyanqing@tyut.edu.cn (Y.Y.)

† Yanrong Zhang contributed equally to this work with Weike Zhang and should be considered co-first authors.

check for updates

Abstract: A silicon dioxide/carbon nano onions/titanium dioxide (SiO$_2$/CNOs/TiO$_2$) composite was synthesized by a simple sol-gel method and characterized by the methods of X-ray diffraction (XRD), scanning electronic microscope (SEM), X-ray photoelectron spectroscopy (XPS), Brunauer–Emmett–Teller (BET), Fourier transform infrared (FTIR), thermogravimetric analysis (TG), differential scanning calorimeter (DSC) and UV-Vis diffuse reflectance spectra (UV-Vis DRS). In this work, the photocatalytic activity of the SiO$_2$/CNOs/TiO$_2$ photocatalyst was assessed by testing the degradation rate of Rhodamine B (RhB) under visible light. The results indicated that the samples exhibited the best photocatalytic activity when the composite consisted of 3% CNOs and the optimum dosage of SiO$_2$/CNOs/TiO$_2$(3%) was 1.5 g/L as evidenced by the highest RhB degradation rate (96%). The SiO$_2$/CNOs/TiO$_2$ composite greatly improved the quantum efficiency of TiO$_2$. This work provides a new option for the modification of subsequent nanocomposite oxide nanoparticles.

Keywords: titanium dioxide; carbon nano onions; silicon dioxide; rhodamine B; photocatalytic degradation

1. Introduction

Industrial dye wastewater is the main source of water pollution. As a triphenylmethane derivative, Rhodamine B is widely used in the manufacture of paints, acrylic fabrics and other biological products due to its bright color and good color-solidity. This dye wastewater is highly toxic to human beings (LD50: Oral-Mouse-887 mg/kg) due to its high chroma, strong toxicity and difficulty in degradation [1–3]. In addition, the low rate of removal during primary and secondary treatments observed in wastewater plants is due to their recalcitrant tendency toward aerobic conditions (emanating from the hard to breakdown compounds, such as aromatic structures) and it results in their easy carry-over into the aqueous ecosystem [4,5]. Recent research efforts have been centered on the development of novel strategies that can eliminate dyes more efficiently and economically. Semiconductor photocatalysis technology is one of the effective means to solve water polluted by organic contaminants [6–8]. As a semiconductor, titanium dioxide (TiO$_2$) is featured by its chemical stability, being environmentally harmless and low cost [9–12]. However, its application in environmental pollution remediation was hampered by some internal defects of TiO$_2$, such as a large band gap, higher recombination of photogenerated e^--h^+ pairs, small surface area and low recovery rate [13–15]. Therefore, the nano-TiO$_2$

were modified to prepare a composite, which may have properties of a low rate of recombination of photogenerated e^--h^+, high surface adsorption and a good recovery rate.

Carbon materials, such as activated carbon, carbon nanotubes, graphene, fullerene materials (C60) and graphene-based material, have been widely used in the field of photocatalysis. These carbon materials can improve photocatalytic activity by facilitating the transfer of photogenerated electrons and enhancing the adsorption performance of the catalyst due to their unique electrical properties and large specific surface area [16–20]. Commercial CNOs prepared by the chemical vapor deposition (CVD) method using iron-nickel as a catalyst exhibit good electrical conductivity and certain paramagnetism [21,22]. Zhang et al. synthesized Bi_2WO_6/MCNOs (MCNOs, magnetic carbon nano onions) via a simple hydrothermal method and reported that the degradation efficiency of RhB by the Bi_2WO_6/MCNOs after six cycles was 87.2% [23]. Meanwhile, our previous research found that the pure TiO_2, CNOs/TiO_2 (10%) composite was more effective in the separation of e^--h^+ and easily recovered by an external magnet (the degradation value of RhB was 78%). The reason for this is that the good electrical conductivity of nano-onion carbon was beneficial to capture photogenerated electrons and could effectively inhibit photogenerated electron-hole pair recombination. In addition, as the paramagnetism of CNOs, the catalyst powder can be recovered by an external magnet [24].

Considering that the specific surface area of CNOs/TiO_2 (263.442 m^2/g) is not significantly improved compared with TiO_2 (255.948 m^2/g), which is not conducive to the adsorption of pollution, the CNOs/TiO_2 composite is further modified to increase its specific surface area. SiO_2 is a typical disordered mesoporous material. Due to its large specific surface area, uniform pore size, stable chemical properties and relatively high mechanical strength, SiO_2 has been widely used in the fields of catalysis, separation and adsorption [25–27]. For example, Yaparatne et al. found that P25 (P25 is a titanium dioxide with an average particle size of 25 nm composed of anatase crystals and rutile crystals) modified TiO_2-SiO_2 photocatalyst films which showed ~80% loss of 2-methylisoborneol (MIB) within 1 h and resulted in ~80% Geosmin (GSM) photodegradation in 1 h, while the major species hydroxyl radicals (•OH) did not change after 10 repetitions [28]. Kim et.al reported that the SBET value of the Cellulose-SiO_2 composite aerogel (CSG, the concentration of SiO_2 was 10 wt %) increased to 355 m^2/g compared with the cellulose aerogel (CG, 216 m^2/g) [29]. In addition, Cui et al. found that the surface area of 600–5% SiO_2-TiO_2 nanofibers (95.96 m^2/g) was nearly 12 times that of 600–0% SiO_2-TiO_2 nanofibers (8.17 m^2/g) (the Si/Ti ratio increased from 0% to 5% and treated at 600 °C) [30].

Herein, in this work, SiO_2/CNOs/TiO_2 photocatalyst was synthesized for the first time via a sol-gel method and was separated from aqueous media using an external magnet. In addition, SiO_2 significantly improved the specific surface area of SiO_2/CNOs/TiO_2 which was 1.87-times larger than that of TiO_2. Moreover, this study explored the photodegradation performance of the SiO_2/CNOs/TiO_2 composite for RhB under visible light and proposed a possible mechanism according to the characterization of the synthesized composite and free radical capture experiments.

2. Materials and Methods

2.1. Materials

Titanium (IV) isopropoxide ($C_{12}H_{28}O_4Ti$), ethanol (C_2H_6O), nitric acid (HNO_3), tetraethyl orthosilicate ($C_8H_{20}O_4Si$), rhodamine B ($C_{28}H_{31}ClN_2O_3$), diacetone alcohol ($C_6H_{12}O_2$), 2-methoxyethanol ($C_3H_8O_2$), sodium sulphate (Na_2SO_4), dimethyl carbinol (C_3H_8O), ethylenediaminetetraacetic acid disodium salt ($C_{10}H_{14}N_2Na_2O_8$), P-19 dispersant and benzoquinone ($C_6H_4O_2$) were purchased from Damao Chemical Reagent Factory (Tianjin, China). All the above chemical reagents were analytical grade. CNOs were purchased from Shanxi Zhongxing Environmental and Energy Technology Co. Ltd. (Shanxi, China). The Brunauer–Emmett–Teller (BET) surface area of the CNOs was 60–80 m^2/g and D50 was 70 nm.

2.2. Synthesis of SiO₂/CNOs/TiO₂

The SiO$_2$/CNOs/TiO$_2$ composite was prepared by the sol-gel method. C$_{12}$H$_{28}$O$_4$Ti and C$_8$H$_{20}$O$_4$Si were used as a titanium resource and silicon resource, respectively. The CNOs were used as functional additives. The target product designed by the authors is a composite of Anatase TiO$_2$ (TiO$_6$ octahedral structure with a coordination number of 6), SiO$_2$ crystal (SiO$_4$ tetrahedral structure with a coordination number of 4) and CNOs. Therefore, the atom ratio of Ti and Si was controlled at 3:2. The products were designated as SiO$_2$/CNOs/TiO$_2$(X), where X was the mass ratio of CNOs to TiO$_2$. The values of X in this experiment were 1%, 2%, 3%, 5% and 10% for five different SiO$_2$/CNOs/TiO$_2$ samples. The detailed steps of synthesis are as follows:

a. CNOs/TiO$_2$ solution: Firstly, 7 mL of C$_{12}$H$_{28}$O$_4$Ti solution was added into 3 mL of C$_3$H$_8$O solution and stirred at room temperature. Secondly, magnetic CNOs were added to the mixed solution. The mixed solution was then transferred dropwise to a round bottom flask containing distilled water at a dropping rate of 0.4 mL/min, when the stir and condensation system were opened. Next, 1 mL of HNO$_3$ solution was added to the mixed solution at a dropping rate of 0.35 mL/min at 80 °C. Finally, CNOs/TiO$_2$ solution was obtained after the solution was cooled to room temperature.

b. SiO$_2$ solution: Firstly, 6 mL of C$_8$H$_{20}$O$_4$Si, 15 mL of C$_2$H$_6$O, 0.35 mL of HNO$_3$ and 0.4 mL of deionized water were thoroughly mixed in a three-neck round bottom flask and stirred for 30 min. Secondly, a certain amount of mixed solution (C$_2$H$_6$O and HNO$_3$) was added to the flask and stirred at 55 ± 3 °C for 2 h. Finally, SiO$_2$ solution was obtained after the solution was cooled to room temperature.

c. SiO$_2$/CNOs/TiO$_2$ composite: Firstly, 26.5 mL of the CNOs/TiO$_2$ solution prepared in Step (a) and 16 mL of the SiO$_2$ solution prepared in Step (b) were mixed and stirred for 30 min. Then, 26 mL of the diluent solution 1 (C$_2$H$_6$O:C$_6$H$_{12}$O$_2$:HNO$_3$:P-19:H$_2$O = 239:31:5:1:49) was added and stirred for 30 min. Next, 42 mL of the diluent solution 2 (C$_2$H$_6$O:C$_3$H$_8$O$_2$:P-19:H$_2$O = 260:67:1:242) was added and stirred for 1 h. Finally, the SiO$_2$/CNOs/TiO$_2$ composite was obtained after the solution was oven-dried at 100 °C.

2.3. Characterization

The morphologies and microstructures of the SiO$_2$/CNOs/TiO$_2$ composite were analyzed using a field-emission scanning electron microscopy (FESEM) (JSM-6700, Joel Ltd., Tokyo, Japan) with an operating voltage of 10 kV. An X-ray diffraction (XRD) analyzer (DX-2700X, Haoyuan Instrument Co., Ltd., Dandong, China) was used to characterize its crystallographic structure and crystallographic composition, with a power set at 40 kV and 30 mA, 2θ ranging from 5° to 80° at a scanning rate of 8°/min with a Cu Kα-radiation wavelength = 1.54184 Å. The functional groups of the samples were analyzed using a Nicolet iS[10] Fourier transform-infrared spectrometer (FTIR) (Nicolet iS[10], Thermo Fisher Scientific, Waltham, MA, USA) in the wavenumber range of 400–4000 cm^{-1}. The Brunauer–Emmett–Teller (BET) surface area and pore distribution were determined using a surface area and porosity analyzer (Quadrasorb SI, Quantachrome instruments, Boynton Beach, FL, USA). The chemical states of the main elements in the photocatalysts were explored by using an X-ray photoelectron spectroscopy (XPS) (Amicus, Shimadzu, Kyoto, Japan). The thermal stability of the samples was tested on a thermogravimetric-differential scanning calorimeter (TG-DSC) (STA449 F3, NETZSCH-Gerätebau GmbH, Selb, Germany). The tests of the optical properties of the samples were carried out on an UV-Vis diffuse reflectance spectrum (UV2550, Shimadzu, Kyoto, Japan). The electrochemical properties were analyzed by using a CHI760E electrochemical workstation which was based on a three-electrode system with a working electrode (ITO slide), an auxiliary electrode (Pt) and a reference electrode (standard calomel electrode (SCE)), while 0.5 mol/L Na$_2$SO$_4$ solution was used as the electrolyte.

2.4. Photocatalytic Degradation Experiments

The light source was a 300 W Xenon (Xe)-lamp with a cutoff filter ($\lambda \geq 420$ nm) and a light-proof box on the outside. Rhodamine B (RhB) was selected to evaluate the photocatalytic activity of the catalytic material. The specific steps were as follows. Firstly, a given amount of the $SiO_2/CNOs/TiO_2$ sample was added to 100 mL of 10 mg/L RhB solution, followed by 10 min ultrasonic dispersion. Then, the mixture was stirred in the dark for 30 min, in which the adsorption-desorption equilibrium was reached between the catalysts and the reactants. Finally, the mixture was stirred using a magnetic stirrer with the Xe-lamp irradiating (120.5–150.0 mW/cm^2 of the photon flux density). Further, 6 mL of the mixture was taken at an interval of 20 min and centrifuged, followed by measuring the absorbance of the supernatant with an ultraviolet spectrophotometer (UV-2102PC, Unico, Princeton, NJ, USA).

Photocatalytic degradation efficiency was calculated by the following equation:

$$D\% = \left[\frac{C_0 - C_t}{C_0} \right] \times 100\% = \left[\frac{A_0 - A_t}{A_0} \right] \times 100\% \tag{1}$$

where C_0 and C_t are the initial concentration (mg/L) and t-time equilibrium concentration (mg/L). A_0 and A_t are the absorbance of original and time t, respectively.

In addition, the total organic carbon (*TOC*) of the solution was tested using a Total Organic Carbon Analyzer (TOC) (TOC-V CPH, Shimadzu, Kyoto, Japan). The mineralization ratio was determined by the following equation [31]:

$$M\% = \left[\frac{TOC_0 - TOC_t}{TOC_0} \right] \times 100\% \tag{2}$$

where TOC_0 and TOC_t are the initial concentration (mg/L) and t-time equilibrium concentration (mg/L), respectively.

3. Results and Discussion

3.1. Characterization of TiO$_2$, SiO$_2$, CNOs and SiO$_2$/CNOs/TiO$_2$(3%)

The morphologies and sizes of the as-prepared samples were observed by scanning electronic microscope (SEM) images. The TiO$_2$ sample was composed of particles with heavy agglomerates as its sizes were 0.5–1 um (Figure 1a). In contrast, the particles of SiO$_2$/CNOs/TiO$_2$ was presented with slight agglomeration as its sizes in 0.1–0.3 um (Figure 1b), indicating the dispersion of SiO$_2$/CNOs/TiO$_2$ improved significantly than pure TiO$_2$. The high dispersion of the as-prepared composite may not only improve its adsorption capacity, but also expose more active sites.
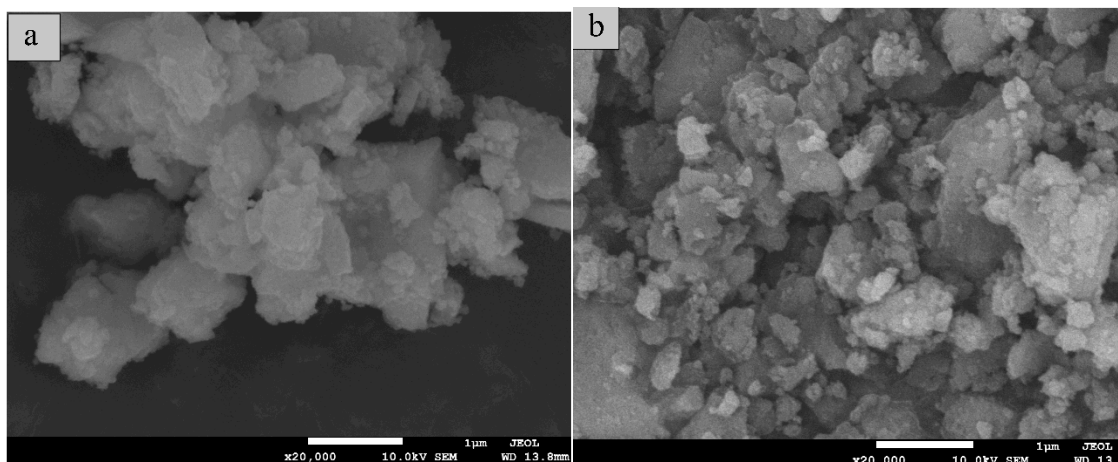

Figure 1. Scanning electronic microscope (SEM) images of (**a**) TiO$_2$ and (**b**) silicon dioxide/carbon nano onions/titanium dioxide (SiO$_2$/CNOs/TiO$_2$(3%)).

The XRD patterns of CNOs, TiO_2, SiO_2 and $SiO_2/CNOs/TiO_2(3\%)$ offered some information about the phase compositions and crystal properties in Figure 2. In Figure 2a, there was an obvious diffraction peak of CNOs at 26.7°, corresponding to the (002) crystal plane of the graphitized cubic crystal [21]. In Figure 2b, the diffraction peaks (25.2° (101), 37.8° (004), 48.1° (200), 53.9° (105), 55.1° (211), 62.7° (204), and 70.3° (220)) were well assigned to the anatase diffraction peaks (PDF#21-1272), indicating that the synthesized TiO_2 was anatase [32]. In Figure 2c, there was a broad peak at 23° of SiO_2, a characteristic peak of amorphous SiO_2, indicating that SiO_2 existed in an amorphous state [33]. In Figure 2d, the diffraction peaks of $SiO_2/CNOs/TiO_2(3\%)$ were similar to those of pure TiO_2, indicating that the form of TiO_2 existed in the composite was anatase.
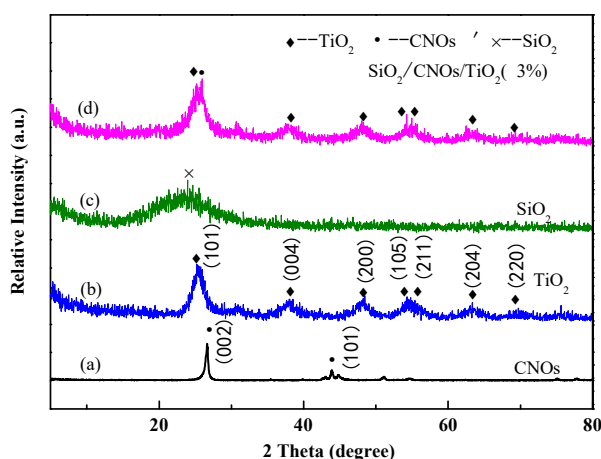

Figure 2. The X-ray diffraction (XRD) patterns of (**a**) CNOs, (**b**) TiO_2, (**c**) SiO_2 and (**d**) $SiO_2/CNOs/TiO_2(3\%)$.

The characteristic diffraction peak at 26.7° belonging to the CNOs (002) crystal plane was also observed, indicating that CNOs effectively combined with TiO_2. However, there were no obvious diffraction peaks of SiO_2 probably due to the amorphous state of SiO_2.

The diffraction peaks at the (104) and (200) crystal planes in TiO_2 were selected to calculate the grain size using the Scherrer formula. These peaks could avoid interference of diffraction peaks between the (101) crystal plane of TiO_2 and the (002) plane of CNOs. As shown in Table 1, the grain size of $SiO_2/CNOs/TiO_2(3\%)$ was smaller than that of TiO_2 and $CNOs/TiO_2$. This finding was consistent with the above SEM images, indicating that the addition of SiO_2 improved the dispersity of the sample.

Table 1. Grain size, surface area, average pore size and pore volume of TiO_2, $CNOs/TiO_2(10\%)$ and $SiO_2/CNOs/TiO_2(3\%)$.

Sample	Grain Size (nm)	Specific Surface Area(m²/g)	Average Pore Size (nm)	Pore Volume (cm³/g)
TiO_2	26.53	255.948	2.348	0.150
$CNOs/TiO_2(10\%)$	23.54	263.442	2.367	0.156
$SiO_2/CNOs/TiO_2(3\%)$	22.55	479.243	3.54	0.305

The BET surface area of the as-prepared $SiO_2/CNOs/TiO_2(3\%)$ was evaluated by the nitrogen adsorption and desorption measurement (Figure 3). The sample showed a type IV isotherm with a H_2 hysteresis loop in Figure 3a, belonging to the porous structure type predominated by mesoporous. Meanwhile, its average pore size was 3.54 nm as presented in the pore size distribution of the $SiO_2/CNOs/TiO_2(3\%)$ composite (Figure 3b), confirming that the sample was a mesoporous structure.
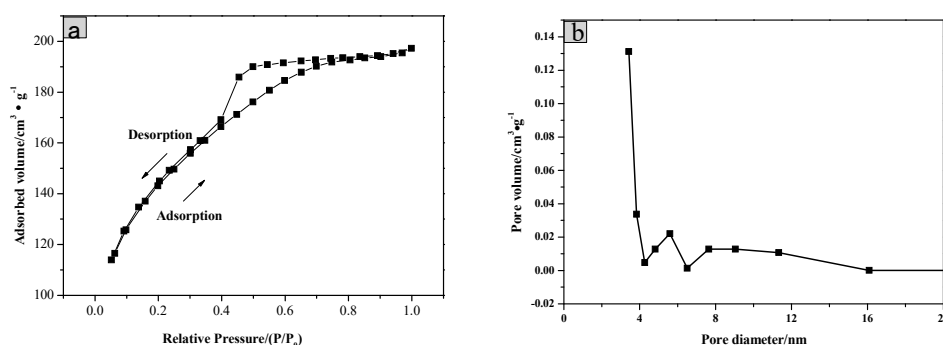
Figure 3. (**a**) Nitrogen adsorption/desorption isotherms and (**b**) pore size distribution of $SiO_2/CNOs/TiO_2(3\%)$.

The specific surface area, average pore size and pore volume of the samples are shown in Table 1. Due to the addition of SiO_2 and CNOs, the specific surface area of $SiO_2/CNOs/TiO_2(3\%)$ was 1.87-times larger than that of TiO_2. The improvement in the specific surface area may be beneficial to pollutant adsorption.

The element composition and valence bond structure of the $SiO_2/CNOs/TiO_2(3\%)$ composite were characterized by XPS analysis. Figure 4 shows the X-ray photoelectron full spectrum of $SiO_2/CNOs/TiO_2(3\%)$ and high-resolution spectra of Ti 2p, C 1s and Si 2p, respectively. For the $SiO_2/CNOs/TiO_2(3\%)$ composite, there were four predominant binding energy peaks at 459 eV, 285 eV, 102 eV and 530 eV, corresponding to the Ti 2p, C 1s, Si 2p and O1s, respectively. In the spectrum of the Ti element (Figure 4b), two characteristic peaks observed at approximately 459.7 eV and 465.1 eV corresponded to Ti^{4+} $2p_{1/2}$ and Ti^{4+} $2p_{3/2}$ in anatase TiO_2, indicating that the Ti element existed as Ti^{4+} in the sample [34]. Meanwhile, the peaks at 460.9 eV and 466.7 eV corresponded to Ti 2p in Ti-O-Si. In the high-resolution spectrum of the C element (Figure 4c), the peaks at the binding energies of 284.6 eV, 283.3 eV and 288.6 eV corresponded to the contamination of the instrument itself, sp^2 hybridization in CNOs or C of Ti–O–C bonds and the C=O in CNOs, respectively [35,36]. There were two peaks at 102.56 eV and 101.66 eV in the high-resolution spectrum of the Si element (Figure 4d), which belonged to the binding energy Si 2p in Si-O-Si and Ti-O-Si, respectively [37]. The XPS results are consistent with the results of the XRD analysis, confirming that the $SiO_2/CNOs/TiO_2(3\%)$ composite was successfully synthetized.

Figure 5 shows the FTIR spectra of TiO_2, CNOs, SiO_2 and $SiO_2/CNOs/TiO_2(3\%)$. The absorption peaks near 3400 cm^{-1} and 1637 cm^{-1} of all the samples may be caused by water molecules in the samples or the stretching vibration of the hydroxyl functional groups [38]. For CNOs (Figure 5a): The characteristic absorption peaks at 2900 cm^{-1} and 2820 cm^{-1} corresponded to the stretching vibration of the methyl and methylene groups; the peak at 1064 cm^{-1} was caused by C–O bond stretching vibration; the peak at 526 cm^{-1} corresponded to the C60 energy band [39,40]. For TiO_2 (Figure 5b), the symmetry stretching vibration peak of the Ti–O–Ti bond was located at 604 cm^{-1} [41], and the bending vibration peak of NO_3^- was located at 1384 cm^{-1} due to the addition of HNO_3 in the material synthesis. In the infrared spectrum of SiO_2 (Figure 5c), the characteristic peaks at 956 cm^{-1} and 1074 cm^{-1} were the symmetric stretching vibration of Si–O–Si and the antisymmetric stretching vibration of Si–O–Si, respectively [42]. For the $SiO_2/CNOs/TiO_2$ (3%) composite (Figure 5d), the characteristic peaks at 1384 cm^{-1}, 664 cm^{-1} and 961 cm^{-1} corresponded to the bending vibration of the C–C bond, the symmetric stretching vibration of Ti–O–Ti bond and the stretching vibration of Si–O–Si, respectively. Meanwhile, the characteristic peak of CNOs at 1064 cm^{-1} was weak due to its overlap with the peak of the antisymmetric stretching vibration of Si-O-Si (1074 cm^{-1}). The results indicated that the composite was successfully synthesized by TiO_2, SiO_2 and CNOs [38–42].
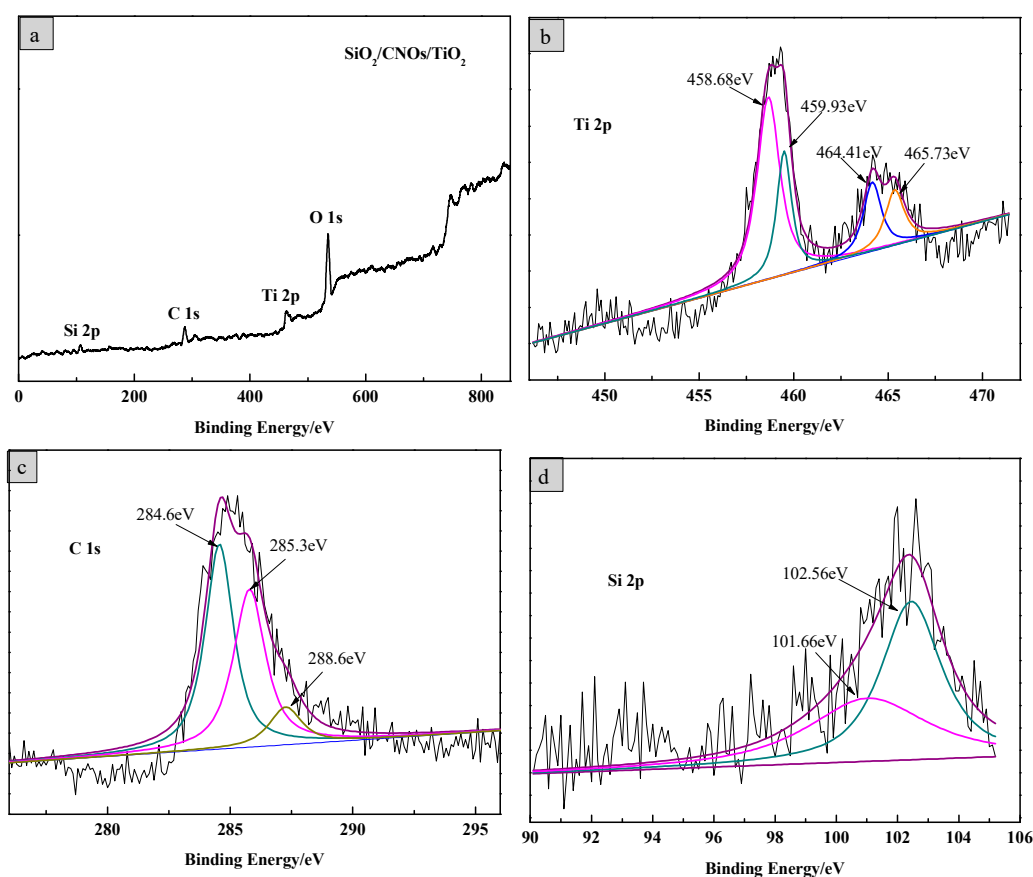
Figure 4. (**a**) X-ray photoelectron spectroscopy (XPS) full spectrum of the SiO_2/CNOs/TiO_2(3%) sample and high-resolution spectra of (**b**) Ti, (**c**) C and (**d**) Si.
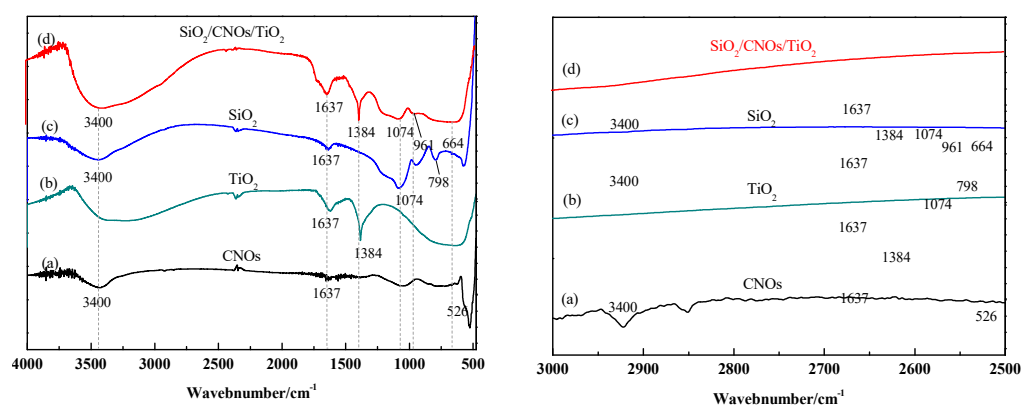

Figure 5. Fourier transform-infrared spectrometer (FTIR) spectra of (**a**) CNOs, (**b**) TiO_2, (**c**) SiO_2 and (**d**) SiO_2/CNOs/TiO_2(3%) and partial enlargement in 3000–2500 cm^{-1}.

The thermal stability of the SiO_2/CNOs/TiO_2(3%) composite was explored by TG-DSC. In Figure 6a, the thermogravimetric analysis (TG) curve of the TiO_2 sample consisted of four parts. Part 1: below 200 °C. The mass loss was 6.23 wt %, derived from moisture evaporation from the TiO_2 surface. Meanwhile, the value of the DSC curve was greater than zero, indicating that the process was an endothermic reaction. Part 2: 200–300 °C. The weight loss was 4.51 wt %, caused by the dihydroxylation process inside the material. During the process, the hydroxyl group combined oxygen to form water. Part 3: 300–600 °C. The weight loss was 7.68%, derived from the oxidative decomposition of organic matter in the sample. Part 4: above 600 °C. The main component in the remaining sample was pure TiO_2 without mass lost [40]. The TG curve of SiO_2/CNOs/TiO_2(3%) was made up of five parts

(Figure 6b). The mass loss of the composite before 600 °C was similar to that of the TiO$_2$ sample, of which the weight loss of evaporation, dihydroxylation and oxidative decomposition of the organic matter were 6.85%, 4.53% and 8.27%, respectively. Between 550 °C and 780 °C, the mass loss of the sample was 0.96%, caused by the thermal decomposition of CNOs in the sample. Above 780 °C, the weight remained stable. The residual was dominated by SiO$_2$ and TiO$_2$ [43]. These results indicated that the thermal stability of the SiO$_2$/CNOs/TiO$_2$(3%) composites was quite good.
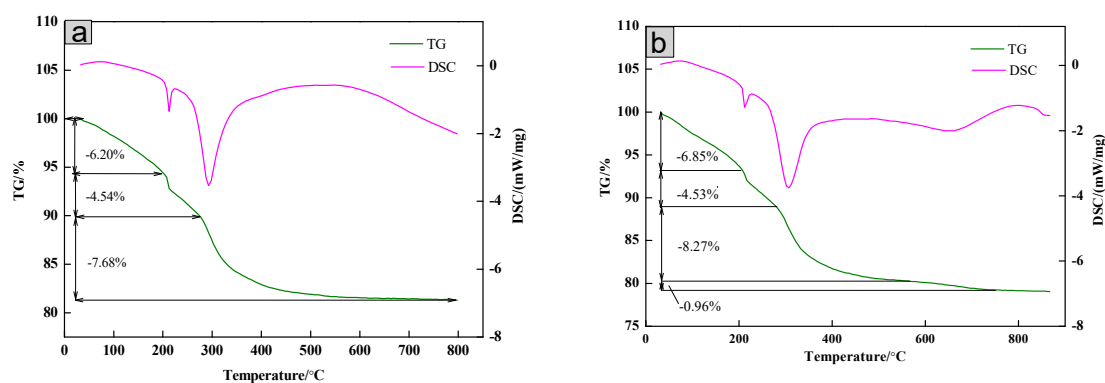

Figure 6. Thermogravimetric-differential scanning calorimeter (TG-DSC) curves of (**a**) TiO$_2$ and (**b**) the SiO$_2$/CNOs/TiO$_2$(3%) composite.

The band gap energies were estimated using the Tauc formula $(\alpha h\nu)^{1/2} \propto (h\nu - Eg)$, where α is the absorption coefficient, ν is the frequency of the light, h is Planck's constant and Eg is the band gap [44,45]. In Figure 7, the absorbance of SiO$_2$/CNOs/TiO$_2$(3%) in the visible region was stronger than TiO$_2$, in which the band gap energies were found to be 2.90 eV and 2.22 eV for TiO$_2$ and SiO$_2$/CNOs/TiO$_2$(3%).
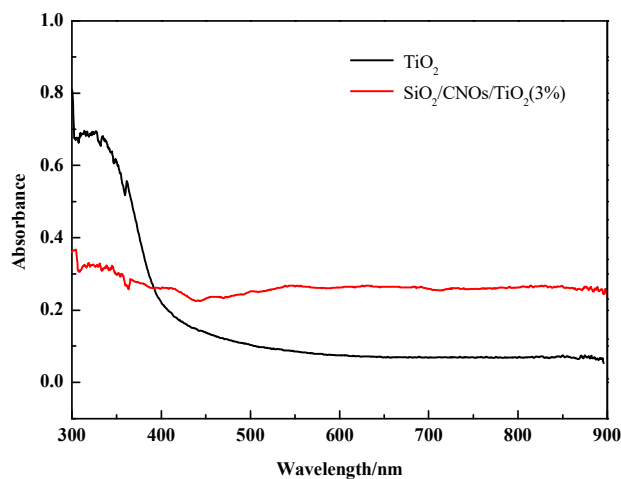

Figure 7. UV-Vis diffuse reflectance spectra of TiO$_2$ and SiO$_2$/CNOs/TiO$_2$(3%).

In addition, the conduction band (CB) and valence band (VB) of TiO$_2$ are calculated by following equations:

$$E^0_{CB} = \chi - E^C - 0.5Eg \tag{3}$$

$$E_{VB} = E_{CB} - Eg \tag{4}$$

where χ is the absolute electronegativity of the semiconductor (χ is 5.81 eV for TiO$_2$), E^C is the energy of free electrons on the hydrogen scale (~4.5 eV) and Eg is the band gap energy of the semiconductor. After calculations, the VB and CB of TiO$_2$ are −3.04 eV and −0.14 eV, respectively. There may be two possible reasons. On the one hand, the addition of CNOs improved the visible light absorption capacity of TiO$_2$ due to its high electrical conductivity [21,22]. On the other hand, the addition of SiO$_2$ enhanced

the dispersibility of the material caused by its large specific surface area and therefore increased the contact rate of the material with photons under visible light [29,30].

3.2. Degradation of RhB under Visible Light Irradiation

Photocatalytic performance was evaluated by measuring the degradation efficiency of RhB (100 mL of 10 mg/L RhB, dosage was 2.0 g/L). Photocatalytic degradation efficiencies of RhB by different ratio CNOs to the SiO_2/CNOs/TiO_2 composites is presented in Figure 8.
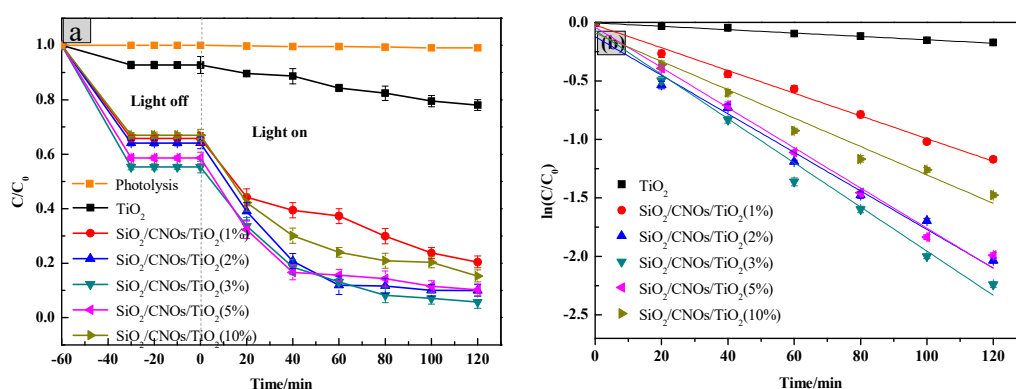

Figure 8. (**a**) Photocatalytic degradation of different CNOs composite ratio and (**b**) linear transform of $\ln(C/C_0) = k \cdot t$ of the kinetic curve of Rhodamine B degradation by the TiO_2/CNOs/ SiO_2 catalysts.

In the dark reaction, all samples reached the adsorption-desorption equilibrium in 30 min and the process could adsorb approximately 35–45% of RhB corresponding to the adsorbed quantities which were 1.634–2.274 mg/L as seen in Figure 8a. This phenomenon may be attributed to the large specific surface area of SiO_2 which was beneficial to the adsorption of pollutants. In the light reaction, compared with the absence of the photocatalyst, the degradation efficiency of RhB significantly improved after the addition of the prepared materials. The low CNOs (<3%) may have a little high recombination of photogenerated e^--h^+ as the e^- could not transfer to CNOs immediately. On the other hand, the high-level CNOs (>3%) may lead the formation of passive layers that lowered the photoadsorption efficiency of SiO_2/CNOs/TiO_2 and reduced the specific surface area. Meanwhile, the degradation efficiency of SiO_2/CNOs/TiO_2(3%) reached the highest value of 94% (Figure 8a), so 3% was selected as the optimal content of CNOs in this work.

To further explore the catalytic reaction, the degradation kinetics of the catalyst with the integrated rate law $\ln(C/C_0) = k \cdot t$ (Figure 8b) was investigated [46]. As shown in Figure 8b, the rate constants k were −0.00148, −0.00956, −0.01714, −0.01815, −0.01638 and −0.01213 min^{-1} for TiO_2, SiO_2/CNOs/TiO_2(1%), SiO_2/CNOs/TiO_2(2%), SiO_2/CNOs/TiO_2(3%), SiO_2/CNOs/TiO_2(5%) and SiO_2/CNOs/TiO_2(10%), respectively. The absolute value of k of SiO_2/CNOs/TiO_2(3%) was largest, which was consistent with the SiO_2/CNOs/TiO_2(3%) composites which exhibited optimal photoactivity.

In order to explore the effect of the sample dosage on photodegradation efficiency, 1.0 g/L, 1.5 g/L, 2.0 g/L, 2.5 g/L and 3.0 g/L of the SiO_2/CNOs/TiO_2(3%) composite were added to 100 mL of 10 mg/L RhB solution, respectively (Figure 9).
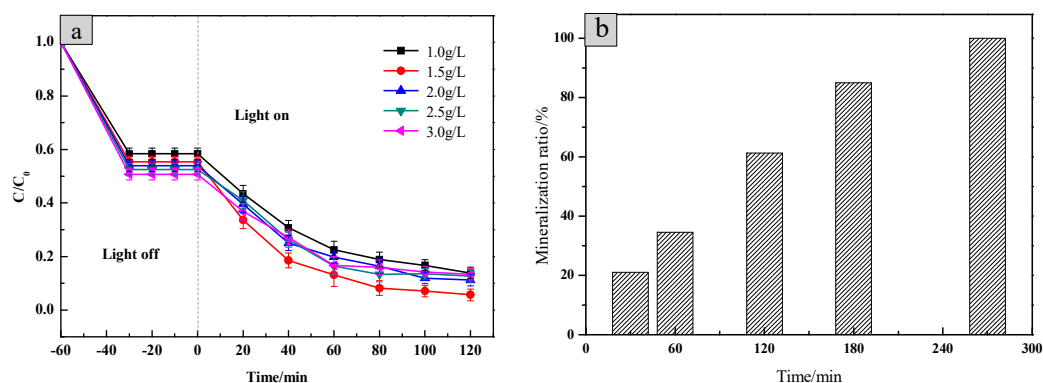
Figure 9. (**a**) The effect of the dosage of $SiO_2/CNOs/TiO_2(3\%)$ on photodegradation efficiency and (**b**) the RhB's mineralization ratio of 1.5 g/L $SiO_2/CNOs/TiO_2(3\%)$ during photocatalytic processes.

At the beginning, the photodegradation efficiency of RhB increased with the increase of the amount of $SiO_2/CNOs/TiO_2(3\%)$. Then, it decreased as the amount of the sample increased continuously, caused by high turbidity in the reaction system and aggregation of the catalyst [23]. The optimum additional amount of $SiO_2/CNOs/TiO_2(3\%)$ was 1.5 g/L as the value of the photodegradation efficiency for RhB reached 96.25% after 120 min under visible light irradiation. To further explore the kinetics of RhB photodegradation, the mineralization ratio by TOC was measured [31]. As shown in Figure 9b, after 120 min and 270 min of irradiation, the mineralization ratio of RhB reached 61.31% and 100%, respectively.

The stability of the $SiO_2/CNOs/TiO_2(3\%)$ was determined by the efficiencies of the repeated degradation of RhB (100 mL of 10 mg/L RhB, dosage was 1.5 g/L). The catalyst material was recovered by applying an external magnet due to the paramagnetism magnetism of CNOs, which was washed several times with distilled water and subsequently dried at 80 °C for 12 h. The degradation efficiency of the recovered catalyst presented in Figure 10 shows that the degradation efficiency of RhB reduced from 96.25% in the initial test to 79.3% after 5 cycles of testing. This may be due to a decrease in the surface-active sites of the catalyst or a mass loss of the catalyst during the recovery process.
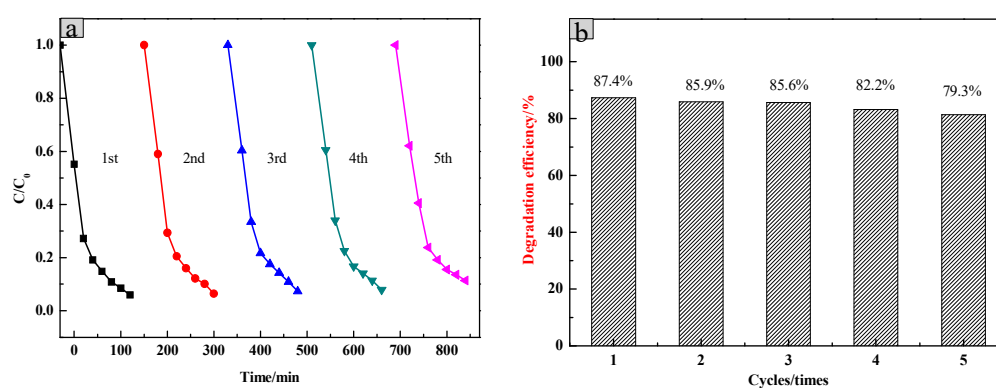

Figure 10. (**a**) The five-run test of photocatalytic activity by using the recovered $SiO_2/CNOs/TiO_2(3\%)$ and (**b**) its degradation efficiency.

Furthermore, in order to investigate the cycle stability of the catalyst, RhB, the newly prepared $SiO_2/CNOs/TiO_2(3\%)$ composite and the five cycles composite were characterized by FTIR, respectively (Figure 11). The intensity and position of the characteristic absorption peak of the two catalysts hardly changed. No other new absorption peak was found in the five cycles of the catalyst indicating that the adsorbed RhB on the photocatalytic material was completely degraded. The above results showed that the $SiO_2/CNOs/TiO_2(3\%)$ composite had good stability.
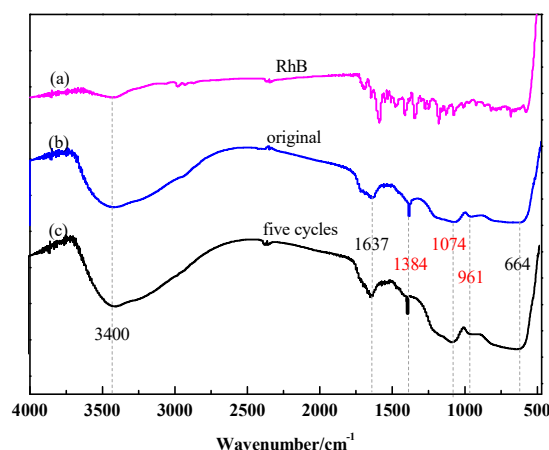
Figure 11. (**a**) The FTIR spectra of RhB, (**b**) original SiO$_2$/CNOs/TiO$_2$(3%) and (**c**) five cycles of the SiO$_2$/CNOs/TiO$_2$(3%).

3.3. Photodegradation Mechanism of the SiO$_2$/CNOs/TiO$_2$(3%) Composite

In order to investigate the role of the different active species in the catalytic system which was generated under visible light irradiation, EDTA-2Na (0.02 g/L) was used to capture h^+. Isopropanol (IPA) (0.02 g/L) was added to capture •OH and benzoquinone (BQ) (0.01 g/L) was adopted to capture •O$_2^-$, respectively [47]. In Figure 12, compared with the original degradation, the degradation efficiency of RhB did not change significantly after adding IPA and EDTA-2Na. However, the efficiency of the photocatalytic degradation reduced from 94% to 60% when BQ was added, indicating that the •O$_2^-$ was the main active species in the photocatalytic degradation process.

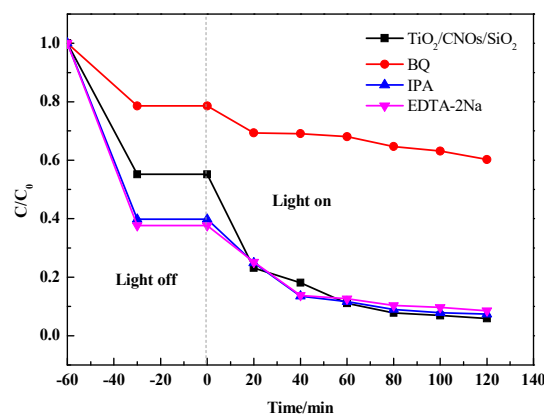**Figure 12.** Reactive species trapping experiments of RhB with the sample SiO$_2$/CNOs/TiO$_2$(3%).

Then, the UV-visible absorption spectrum of RhB solutions with different degradation time was measured. In Figure 13, the reaction time was extended until the RhB solution degraded and became colorless with the optimum dosage of 1.5 g/L. It can be seen from the figure that the intensity of the largest characteristic absorption peak at 554 nm was significantly weakened and its position was blue-shifted within the progress. The entire degradation process took 150 min, in which the color of the RhB solution changed from pink to light yellow, and finally to colorless.
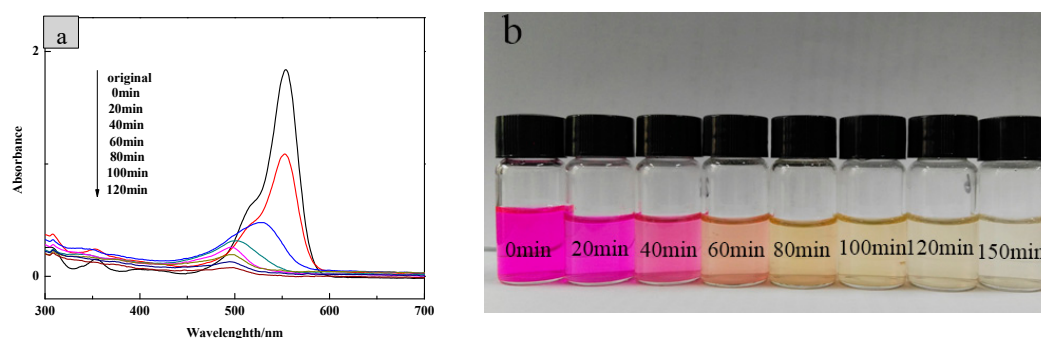
Figure 13. (**a**) UV-vis scanning of different degradation time of RhB solution and (**b**) the color change of RhB during photodegradation.

In addition, the excitation and migration of photogenerated carriers during photocatalysis was explored by photochemical tests. In Figure 14a, for the $SiO_2/CNOs/TiO_2(3\%)$ composite, the value of photocurrent response did not change significantly after several tests, indicating that the photocurrent response of the material was stable. Meanwhile, the prepared sample showed a higher photocurrent intensity than TiO_2 when the light source was turned on, indicating that the composite enhanced the separation efficiency of electrons and holes [48].
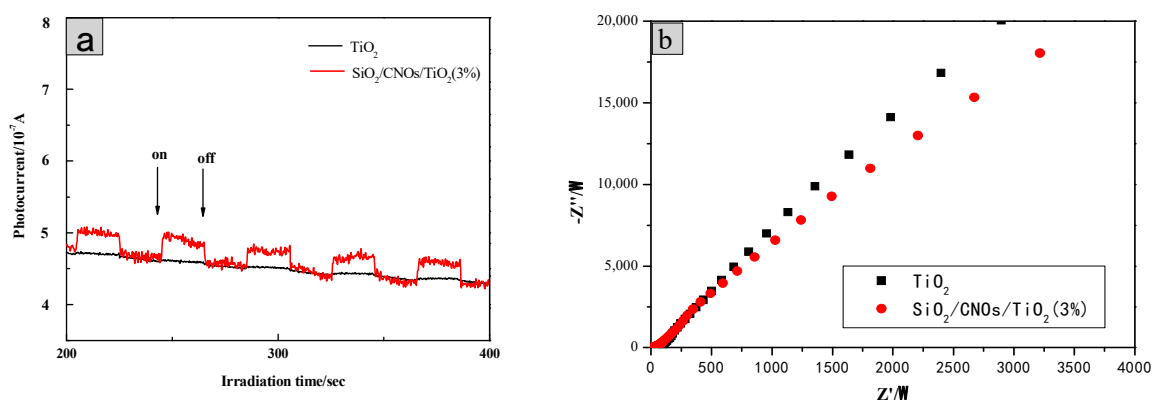

Figure 14. (**a**) Time-based photocurrent responses of samples and (**b**) Nyquist plots.

The electron mobility of photocatalytic materials was further studied according to an electrochemical impedance spectroscopy (EIS) test (Figure 14b. The charge transport resistance of the $SiO_2/CNOs/TiO_2(3\%)$ material was smaller than that of TiO_2 as the radius of $SiO_2/CNOs/TiO_2(3\%)$ was smaller, increasing the electron migration rate and reducing the recombination probability of photogenerated e^--h^+ pairs.

Based on the above results, the photocatalytic degradation mechanism of the $SiO_2/CNOs/TiO_2(3\%)$ composite may be elucidated as follows. First, the BET surface area of the $SiO_2/CNOs/TiO_2(3\%)$ sample was 1.94-times larger than that of the pure TiO_2 (Table 1), benefitting the adsorption of RhB in a dark reaction and the contact between catalysts and contaminants. Then, after N-deethylation of RhB, the opening ring process began with the formation of oxides and small molecule compounds, which were further mineralized into Cl^-, CO_2, NO_3^-, NH_4^+ and H_2O [49,50]. Figure 15 shows the reactions that may occur during photocatalysis. For the $SiO_2/CNOs/TiO_2(3\%)$ composite under light irradiation, the electrons (*e*) are excited and transfer from the valence band (VB) to the conduction band (CB), forming e^--h^+ pairs that travel to the catalyst surface. The band gap energy was 2.22 eV of $SiO_2/CNOs/TiO_2(3\%)$ (Figure 7). As CNOs have good conductivity, photogenerated electrons of the prepared composite transferred to CNOs and reacted with O_2 in the pollutants to form superoxide anion $\bullet O_2^-$ (main active species), resulting in the separation of photogenerated electrons from holes [51]. Moreover, due to

the high surface content of the Ti–O–Si species (formed between TiO_2 and SiO_2), which improved dispersion effectively, the photocatalytic degradation of RhB was significantly enhanced [52].
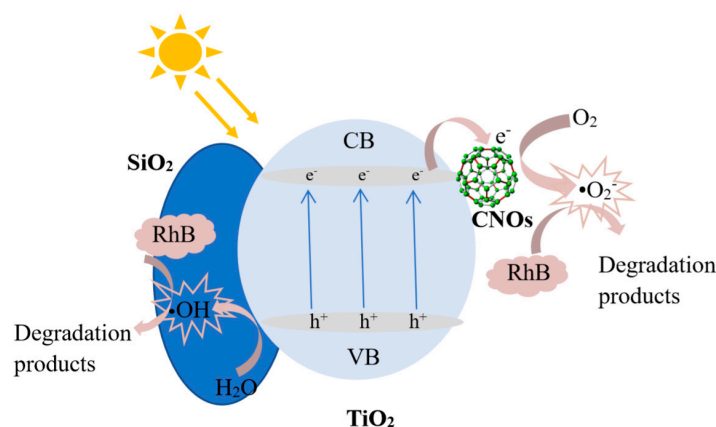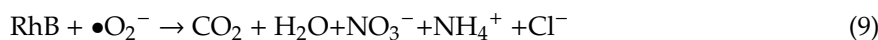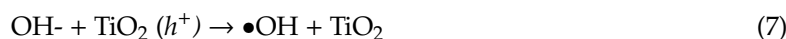

Figure 15. The mechanism diagram of $SiO_2/CNOs/TiO_2$(3%) in the degradation of dyes in visible light.

The reactions that occurred in this process were as follows.

$$SiO_2/CNOs/TiO_2(3\%) + h\nu \rightarrow SiO_2/CNOs(e^-)/TiO_2 (h^+) \tag{5}$$

$$TiO_2 (h^+) + H_2O \rightarrow \bullet OH + H^+ + TiO_2 \tag{6}$$

$$OH\text{-} + TiO_2 (h^+) \rightarrow \bullet OH + TiO_2 \tag{7}$$

$$O_2 + CNOs (e^-) \rightarrow \bullet O_2^- \tag{8}$$

$$RhB + \bullet O_2^- \rightarrow CO_2 + H_2O + NO_3^- + NH_4^+ + Cl^- \tag{9}$$

4. Conclusions

The $SiO_2/CNOs/TiO_2$(3%) composite was successfully prepared by a sol-gel method with a large surface area of 497 m^2/g. The good electrical conductivity of CNOs and the strong adsorption properties of SiO_2 benefited the migration of electrons and separation efficiency of the photo-generated e^--h^+ pairs. When the compounding amount of CNOs was 3% and the dosage was 1.5 g/L, the composite showed the highest photocatalytic activity, where the degradation rate of RhB reached 96.25%. In addition, due to the paramagnetism of the CNOs, the powders can be easily recovered from the aqueous solution using an external magnet. Furthermore, the possible photocatalytic mechanism of the $SiO_2/CNOs/TiO_2$(3%) composite was proposed based on the all experiments. This work may provide a new insight to improve the performance of photocatalysts.

Author Contributions: Conceptualization and funding acquisition, W.Z.; investigation, formal analysis and writing—original draft, Y.Z.; software and validation, J.J. and L.G.; conceptualization, supervision and writing—review and editing K.Y. and Y.Y.

Conflicts of Interest: The authors declare no conflicts of interest.

References

1.   Vikrant, K.; Giri, B.S.; Raza, N.; Roy, K.; Kim, K.-H.; Rai, B.N.; Singh, R.S. Recent advancements in bioremediation of dye: Current status and challenges. *Bioresour. Technol.* **2018**, *253*, 355–367. [CrossRef] [PubMed]

2. Rochkind, M.; Pasternak, S.; Paz, Y. Using Dyes for Evaluating Photocatalytic Properties: A Critical Review. *Molecules* **2015**, *20*, 88–110. [CrossRef]

3. Hurd, T.M.; Brookhart-Rebert, A.; Feeney, T.P.; Otz, M.H.; Otz, I. Fast, regional conduit flow to an exceptional-value spring-fed creek: Implications for source-water protection in mantled karst of south-central Pennsylvania. *J. Cave Karst Stud.* **2013**, *31*, 66–70.

4. Girgis, B.; Attia, A.; Fathy, N.; Attia, A. Potential of nano-carbon xerogels in the remediation of dye-contaminated water discharges. *Desalination* **2011**, *265*, 169–176. [CrossRef]

5. Shouman, M.A.; Fathy, N.A. Microporous nanohybrids of carbon xerogels and multi-walled carbon nanotubes for removal of rhodamine B dye. *J. Water Process. Eng.* **2018**, *23*, 165–173. [CrossRef]

6. Naldoni, A.; Altomare, M.; Zoppellaro, G.; Liu, N.; Kment, Š.; Zbořil, R.; Schmuki, P. Photocatalysis with Reduced TiO_2: From Black TiO_2 to Cocatalyst-Free Hydrogen Production. *ACS Catal.* **2019**, *9*, 345–364. [CrossRef]

7. Shiraishi, Y.; Imai, J.; Yasumoto, N.; Sakamoto, H.; Tanaka, S.; Ichikawa, S.; Hirai, T. Doping of Nb^{5+} Species at the Au–TiO_2 Interface for Plasmonic Photocatalysis Enhancement. *Langmuir* **2019**, *35*, 5455–5462. [CrossRef]

8. Ariza-Tarazona, M.C.; Villarreal-Chiu, J.F.; Barbieri, V.; Siligardi, C.; Cedillo-González, E.I. New strategy for microplastic degradation: Green photocatalysis using a protein-based porous N-TiO_2 semiconductor. *Ceram. Int.* **2019**, *45*, 9618–9624. [CrossRef]

9. Nakata, K.; Kagawa, T.; Sakai, M.; Liu, S.; Ochiai, T.; Sakai, H.; Murakami, T.; Abe, M.; Fujishima, A. Preparation and Photocatalytic Activity of Robust Titania Monoliths for Water Remediation. *ACS Appl. Mater. Interfaces* **2013**, *5*, 500–504. [CrossRef]

10. Rioult, M.; Magnan, H.; Stanescu, D.; Barbier, A. Single Crystalline Hematite Films for Solar Water Splitting: Ti-Doping and Thickness Effects. *J. Phys. Chem. C* **2014**, *118*, 3007–3014. [CrossRef]

11. Pu, A.; Deng, J.; Li, M.; Gao, J.; Zhang, H.; Hao, Y.; Zhong, J.; Sun, X. Coupling Ti-doping and oxygen vacancies in hematite nanostructures for solar water oxidation with high efficiency. *J. Mater. Chem. A* **2014**, *2*, 2491–2497. [CrossRef]

12. Luan, Y.; Jing, L.; Xie, Y.; Sun, X.; Feng, Y.; Fu, H. Exceptional Photocatalytic Activity of 001-Facet-Exposed TiO_2 Mainly Depending on Enhanced Adsorbed Oxygen by Residual Hydrogen Fluoride. *ACS Catal.* **2013**, *3*, 1378–1385. [CrossRef]

13. Cai, J.; Wu, X.; Li, Y.; Lin, Y.; Yang, H.; Li, S. Noble metal sandwich-like TiO_2@Pt@C_3N_4 hollow spheres enhance photocatalytic performance. *J. Colloid Interface Sci.* **2018**, *514*, 791–800. [CrossRef] [PubMed]

14. Ong, W.-J.; Tan, L.-L.; Chai, S.-P.; Yong, S.-T.; Mohamed, A.R. Highly reactive {001} facets of TiO_2-based composites: Synthesis, formation mechanism and characterization. *Nanoscale* **2014**, *6*, 1946–2008. [CrossRef] [PubMed]

15. Sclafani, A.; Herrmann, J.M. Comparison of the Photoelectronic and Photocatalytic Activities of Various Anatase and Rutile Forms of Titania in Pure Liquid Organic Phases and in Aqueous Solutions. *J. Phys. Chem.* **1996**, *100*, 13655–13661. [CrossRef]

16. Wang, X.; Song, J.; Huang, J.; Zhang, J.; Wang, X.; Ma, R.; Wang, J.; Zhao, J. Activated carbon-based magnetic TiO_2 photocatalyst codoped with iodine and nitrogen for organic pollution degradation. *Appl. Surf. Sci.* **2016**, *390*, 190–201. [CrossRef]

17. Aqeel, M.; Anjum, S.; Imran, M.; Ikram, M.; Majeed, H.; Naz, M.; Ali, S.; Ahmad, M.A. TiO_2 @ RGO (reduced graphene oxide) doped nanoparticles demonstrated improved photocatalytic activity. *Mater. Res. Express* **2019**, *6*, 086215. [CrossRef]

18. Zhang, W.; Li, G.; Liu, H.; Chen, J.; Ma, S.; An, T. Micro/nano-bubble assisted synthesis of Au/TiO_2@CNTs composite photocatalyst for photocatalytic degradation of gaseous styrene and its enhanced catalytic mechanism. *Environ. Sci. Nano* **2019**, *6*, 948–958. [CrossRef]

19. Yang, Y.; Zhang, W.; Liu, R.; Cui, J.; Deng, C. Preparation and photocatalytic properties of visible light driven Ag-AgBr-RGO composite. *Sep. Purif. Technol.* **2018**, *190*, 278–287. [CrossRef]

20. Regulska, E.; Rivera-Nazario, D.M.; Karpinska, J.; Plonska-Brzezinska, M.E.; Echegoyen, L. Zinc Porphyrin-Functionalized Fullerenes for the Sensitization of Titania as a Visible-Light Active Photocatalyst: River Waters and Wastewaters Remediation. *Molecules* **2019**, *24*, 1118. [CrossRef]

21. Zhang, W.-K.; Fu, J.-J.; Chang, J.; Zhang, M.; Yang, Y.-Q.; Gao, L.-Z. Fabrication and purification of carbon nano onions. *Carbon* **2015**, *82*, 610. [CrossRef]

22. Zhang, W.; Deng, C.; Jia, J.; Wang, J.; Zhang, Y.; Yang, Y.; Lian, Y. Efficient removal of transition phase from metal encapsulated carbon onions. *Diam. Relat. Mater.* **2018**, *89*, 282–285. [CrossRef]

23. Zhang, W.; Wang, J.; Yang, Y.; Liang, Y.; Gao, Z. Novel magnetically retrievable Bi$_2$WO$_6$/magnetic carbon nano-onions composite with enhanced photoactivity under visible light. *J. Colloid Interface Sci.* **2018**, *531*, 502–512. [CrossRef]

24. Zhang, Y.R.; Zhang, W.K.; Yang, K.; Yang, Y.Q.; Jia, J.; Liang, Y.; Guo, L.J. Carbon nano-onions (CNOs)/TiO$_2$ composite preparation and its photocatalytic performance under visible light irradiation. *J. Environ. Eng.* **2019**, in press. [CrossRef]

25. Zhao, X.; Ju, W.; Zhang, J.; Liu, B.; Zhang, J.; Yi, X. Mesoporous TiO$_2$/SiO$_2$/Ag ternary composite aerogels for high photocatalysis. *New J. Chem.* **2019**, *43*, 6234–6241. [CrossRef]

26. Fang, Y.; Lakey, P.S.J.; Riahi, S.; McDonald, A.T.; Shrestha, M.; Tobias, D.J.; Shiraiwa, M.; Grassian, V.H. A molecular picture of surface interactions of organic compounds on prevalent indoor surfaces: Limonene adsorption on SiO$_2$. *Chem. Sci.* **2019**, *10*, 2906–2914. [CrossRef]

27. Sun, J.; Bi, H.; Su, S.; Jia, H.; Xie, X.; Sun, L. One-step preparation of GO/SiO$_2$ membrane for highly efficient separation of oil-in-water emulsion. *J. Membr. Sci.* **2018**, *553*, 131–138. [CrossRef]

28. Yaparatne, S.; Tripp, C.P.; Amirbahman, A. Photodegradation of taste and odor compounds in water in the presence of immobilized TiO$_2$-SiO$_2$ photocatalysts. *J. Hazard. Mater.* **2018**, *346*, 208–217. [CrossRef]

29. Kim, U.-J.; Kimura, S.; Wada, M. Facile preparation of cellulose-SiO$_2$ composite aerogels with high SiO$_2$ contents using a LiBr aqueous solution. *Carbohydr. Polym.* **2019**, *222*, 114975. [CrossRef]

30. Cui, L.; Song, Y.; Wang, F.; Sheng, Y.; Zou, H. Electrospinning synthesis of SiO$_2$-TiO$_2$ hybrid nanofibers with large surface area and excellent photocatalytic activity. *Appl. Surf. Sci.* **2019**, *488*, 284–292. [CrossRef]

31. Isari, A.A.; Payan, A.; Fattahi, M.; Jorfi, S.; Kakavandi, B. Photocatalytic degradation of rhodamine B and real textile wastewater using Fe-doped TiO$_2$ anchored on reduced graphene oxide (Fe-TiO$_2$/rGO): Characterization and feasibility, mechanism and pathway studies. *Appl. Surf. Sci.* **2018**, *462*, 549–564. [CrossRef]

32. Ren, L.; Li, Y.; Mao, M.; Lan, L.; Lao, X.; Zhao, X. Significant improvement in photocatalytic activity by forming homojunction between anatase TiO$_2$ nanosheets and anatase TiO$_2$ nanoparticles. *Appl. Surf. Sci.* **2019**, *490*, 283–292. [CrossRef]

33. Matysiak, W.; Tański, T. Analysis of the morphology, structure and optical properties of 1D SiO$_2$ nanostructures obtained with sol-gel and electrospinning methods. *Appl. Surf. Sci.* **2019**, *489*, 34–43. [CrossRef]

34. Prokes, S.; Gole, J.; Chen, X.B.; Burda, C.; Carlos, W.E. Defect-Related Optical Behavior in TiO$_2$ Nanostructures. *Adv. Funct. Mater.* **2005**, *15*, 161–167. [CrossRef]

35. Liu, B.; Zeng, H.C. Carbon Nanotubes Supported Mesoporous Mesocrystals of Anatase TiO$_2$. *Chem. Mater.* **2008**, *20*, 2711–2718. [CrossRef]

36. Hung, M.-C.; Yuan, S.-Y.; Hung, C.-C.; Cheng, C.-L.; Ho, H.-C.; Ko, T.-H. Effectiveness of ZnO/carbon-based material as a catalyst for photodegradation of acrolein. *Carbon* **2014**, *66*, 93–104. [CrossRef]

37. Netterfield, R.P.; Martin, P.J.; Pacey, C.G.; Sainty, W.G.; Mc Kenzie, D.; Auchterlonie, G. Ion-assisted deposition of mixed TiO$_2$-SiO$_2$ films. *J. Appl. Phys.* **1989**, *66*, 1805–1809. [CrossRef]

38. Soler-Illia, G.J.D.A.A.; Louis, A.; Sanchez, C. Synthesis and Characterization of Mesostructured Titania-Based Materials through Evaporation-Induced Self-Assembly. *Chem. Mater.* **2002**, *14*, 750–759. [CrossRef]

39. Mykhailiv, O.; Imierska, M.; Petelczyc, M.; Echegoyen, L.; Plonska-Brzezinska, M.E.; Plonska-Brzezinska, M.E. Chemical versus Electrochemical Synthesis of Carbon Nano-onion/Polypyrrole Composites for Supercapacitor Electrodes. *Chem. Eur. J.* **2015**, *21*, 5783–5793. [CrossRef]

40. Mykhailiv, O.; Zubyk, H.; Brzezinski, K.; Gras, M.; Lota, G.; Gniadek, M.; Romero, E.; Echegoyen, L.; Plonska-Brzezinska, M.E. Improvement of the Structural and Chemical Properties of Carbon Nano-onions for Electrocatalysis. *ChemNanoMat* **2017**, *3*, 583–590. [CrossRef]

41. Liu, G.; Chen, Z.-G.; Dong, C.; Zhao, Y.; Li, F.; Lu, G.Q.; Cheng, H.-M. Visible Light Photocatalyst: Iodine-Doped Mesoporous Titania with a Bicrystalline Framework. *J. Phys. Chem. B* **2006**, *110*, 20823–20828. [CrossRef]

42. Hou, Y.; Wang, X.; Wu, L.; Chen, X.; Ding, Z.; Wang, X.; Fu, X. N-Doped SiO$_2$/TiO$_2$ mesoporous nanoparticles with enhanced photocatalytic activity under visible-light irradiation. *Chemosphere* **2008**, *72*, 414–421. [CrossRef]

43. Li, H.; Zhang, Y.; Wang, S.; Wu, Q.; Liu, C. Study on nanomagnets supported TiO$_2$ photocatalysts prepared by a sol–gel process in reverse microemulsion combining with solvent-thermal technique. *J. Hazard. Mater.* **2009**, *169*, 1045–1053. [CrossRef]

44. Suresh, S.; Lekshmi, G.; Kirupha, S.; Ariraman, M.; Bazaka, O.; Levchenko, I.; Bazaka, K.; Mandhakini, M.; Mohandas, M. Superhydrophobic fluorine-modified cerium-doped mesoporous carbon as an efficient catalytic platform for photo-degradation of organic pollutants. *Carbon* **2019**, *147*, 323–333. [CrossRef]

45. Zimnyakov, D.A.; Sevrugin, A.V.; Yuvchenko, S.A.; Fedorov, F.S.; Tretyachenko, E.V.; Vikulova, M.A.; Kovaleva, D.S.; Krugova, E.Y.; Gorokhovsky, A.V. Data on energy-band-gap characteristics of composite nanoparticles obtained by modification of the amorphous potassium polytitanate in aqueous solutions of transition metal salts. *Data Brief* **2016**, *7*, 1383–1388. [CrossRef]

46. Huang, Y.Z.; Chen, D.P.; Hu, X.L.; Qian, Y.J.; Li, D.X. Preparation of TiO$_2$/Carbon Nanotubes/Reduced Graphene Oxide Composites with Enhanced Photocatalytic Activity for the Degradation of Rhodamine B. *Nanomaterials* **2018**, *8*, 431. [CrossRef]

47. Monteagudo, J.; Durán, A.; Martín, I.S.; Carrillo, P. Effect of sodium persulfate as electron acceptor on antipyrine degradation by solar TiO$_2$ or TiO$_2$/rGO photocatalysis. *Chem. Eng. J.* **2019**, *364*, 257–268. [CrossRef]

48. Zhao, J.; Wu, T.; Wu, K.; Oikawa, K.; Hidaka, H.; Serpone, N. Photoassisted Degradation of Dye Pollutants. 3. Degradation of the Cationic Dye Rhodamine B in Aqueous Anionic Surfactant/TiO$_2$ Dispersions under Visible Light Irradiation: Evidence for the Need of Substrate Adsorption on TiO$_2$ Particles. *Environ. Sci. Technol.* **1998**, *32*, 2394–2400. [CrossRef]

49. Chen, C.; Liu, X.; Long, H.; Ding, F.; Liu, Q.; Chen, X. Preparation and photocatalytic performance of graphene Oxide/WO$_3$ quantum Dots/TiO$_2$@SiO$_2$ microspheres. *Vacuum* **2019**, *164*, 66–71. [CrossRef]

50. Shi, F.; Liu, J.; Liu, J.X.; Huang, X.; Hu, S.C.; Liu, D.Y.; Wang, Y.Q.; Shan, Z.J. Influences of solvothermal-assisted crystallization process on the microstructure and properties of SiO$_2$-W$_{0.02}$TiO$_{2.06}$ composite aerogels synthesized via ambient pressure drying. *J. Sol-Gel Sci. Technol.* **2019**, *92*, 101–115. [CrossRef]

51. Liddell, P.A.; Kuciauskas, D.; Sumida, J.P.; Nash, B.; Nguyen, D.; Moore, A.L.; Moore, T.A.; Gust, D. Photoinduced Charge Separation and Charge Recombination to a Triplet State in a Carotene−Porphyrin−Fullerene Triad. *J. Am. Chem. Soc.* **1997**, *119*, 1400–1405. [CrossRef]

52. Rasalingam, S.; Kibombo, H.S.; Wu, C.-M.; Budhi, S.; Peng, R.; Baltrusaitis, J.; Koodali, R.T. Influence of Ti–O–Si hetero-linkages in the photocatalytic degradation of Rhodamine B. *Catal. Commun.* **2013**, *31*, 66–70. [CrossRef]